



Universiteit  
Leiden  
The Netherlands

## Visualizing strongly-correlated electrons with a novel scanning tunneling microscope

Battisti, I.

### Citation

Battisti, I. (2019, May 8). *Visualizing strongly-correlated electrons with a novel scanning tunneling microscope*. *Casimir PhD Series*. Retrieved from <https://hdl.handle.net/1887/72410>

Version: Not Applicable (or Unknown)

License: [Leiden University Non-exclusive license](#)

Downloaded from: <https://hdl.handle.net/1887/72410>

**Note:** To cite this publication please use the final published version (if applicable).

Cover Page



Universiteit Leiden



The handle <http://hdl.handle.net/1887/72410> holds various files of this Leiden University dissertation.

**Author:** Battisti, I.

**Title:** Visualizing strongly-correlated electrons with a novel scanning tunneling microscope

**Issue Date:** 2019-05-08

# 5

## Poor electronic screening in lightly doped Mott insulators

This chapter has been published as:  
Battisti *et al.*, Phys. Rev. B **95**, 235141 (2017).

## 5.1 Introduction

One of the unsolved mysteries that we encountered in chapter 4 is that the effective Mott gap measured by scanning tunneling microscopy in the very lightly doped Mott insulator  $(\text{Sr}_{1-x}\text{La}_x)_2\text{IrO}_4$  differs greatly from values reported by photoemission spectroscopy and optical experiments [71, 73, 78, 79].

In the present chapter, we focus on this observation. We attribute its origin to poor electronic screening of the tip-induced electric field in the sample. This phenomenon is well known from STM experiments on semiconductors and goes under the name of tip-induced band bending (TIBB) [49, 50]. In principle, TIBB can affect measurements of all materials with poor electronic screening, including Mott insulators. Indeed, signatures of TIBB are observed for the lightly hole-doped oxychloride  $\text{Ca}_2\text{CuO}_2\text{Cl}_2$  [103], and poor electronic screening effects around charged impurities are observed for Fe dopants in the topological insulator  $\text{Bi}_2\text{Se}_3$  [115], for Co adatoms in graphene [116] and possibly for chiral defects in  $\text{Sr}_3\text{Ir}_2\text{O}_7$  [98, 117]. TIBB has also been discussed for 2D transition metal dichalcogenides [118] and for graphene systems [119]. However, other than in semiconductors and especially with respect to Mott insulators, the effects of TIBB have not been analyzed in much detail.

Here, we develop a model for TIBB specifically for lightly doped Mott insulators. When applied to the iridate  $(\text{Sr}_{1-x}\text{La}_x)_2\text{IrO}_4$ , the model is able to retrieve the intrinsic energy gap from the measured STM data, obtaining a value that reconciles with literature. In general, this model allows us to better understand the physics of the material, and to provide new insights for STM experiments on lightly doped Mott insulators.

We begin with an overview of the phenomenon of TIBB in Sec. 5.2. We start from its basics in semiconductor physics, and we discuss differences and similarities between Mott insulators and semiconductors with respect to the problem of electric field penetration. Section 5.3 is the core of the chapter. Here, we show clear indications of electric field penetration in the iridate samples, and we develop an algorithm to retrieve the intrinsic energy gap from the measured STM gap. Finally, in Sec. 5.4, we show a different manifestation of TIBB in the iridate samples, appearing at doping  $x \approx 5\%$ .

## 5.2 Poor electronic screening and tip-induced band bending

A good measure of how efficiently mobile charges inside a material can screen an externally applied electric field, is given by the screening length  $\lambda_s$ . When a charge

$q$  is added to an electron liquid, its Coulomb potential  $\phi(r)$  is screened as  $\phi(r) = q/r \cdot e^{-r/\lambda_s}$ . In metals like copper, the charge potential is almost perfectly screened since  $\lambda_s = 0.5 \text{ \AA}$ , whereas, in less conducting materials,  $\lambda_s$  can be higher by a few orders of magnitude. In semiconductors, it is typically of the order of 10 nm [120, 121].

As illustrated in Sec. 2.4, Fig. 2.5, poor electronic screening is very detrimental for STM experiments performed on semiconductors. In contrast to metallic samples, here the electric field generated by the tip can partially penetrate the surface, causing an additional potential drop inside the material. This can strongly affect the interpretation of STM data. For instance, the gap measured with tunneling spectroscopy can significantly differ from the intrinsic bandgap in the density of states of the sample, as it has been observed, e.g., on the surfaces of Ge(111) [48],  $\text{FeS}_2(100)$  [122] and  $\text{ZnO}(110)$  [123]. Moreover, TIBB can cause the ionization of donors/acceptors in the semiconductor [124–126], an effect that has been used in tip-induced quantum dot experiments [120].

In all these cases, being able to quantitatively calculate the band bending potential  $\varphi_{\text{BB}}$  at the surface is necessary for the correct interpretation of STM data: only if the value of  $\varphi_{\text{BB}}$  is known, the intrinsic bandgap can be retrieved from the data, and the binding energies of the donors/acceptors can be extracted. For semiconductors, this is often done with a Poisson's equation solver developed by Feenstra [51], that uses the known dielectric constant and carrier concentration. This treatment yields apparent bandgaps  $\approx 15\text{--}20\%$  larger than the intrinsic ones [48, 122].

While Mott insulators share the reduced ability to screen electric fields with semiconductors, their underlying physics is radically different due to the strong electron-electron correlations (see Sec. 1.2). As a consequence, several material parameters that are easily accessible in semiconductors, such as the number of carriers, are difficult to estimate for a (lightly doped) Mott insulator. The models developed for calculating  $\varphi_{\text{BB}}$  in semiconductors can therefore not be applied to Mott insulators. In the following, we develop a model of electric field penetration in the absence of free carriers specifically for lightly doped Mott insulators.

### 5.3 Influence of poor screening on the energy gap of $(\text{Sr}_{1-x}\text{La}_x)_2\text{IrO}_4$

We now concentrate on the lightly doped Mott insulator  $(\text{Sr}_{1-x}\text{La}_x)_2\text{IrO}_4$  at doping levels  $x < 4\%$ . The physics of the material has been thoroughly discussed in chapter 4, and all the experimental conditions are the same. In section 4.5, we left the open mystery that the gap in the sample LDOS as measured with STM is significantly bigger, and thus in disagreement with the one reported by other techniques. Here, we

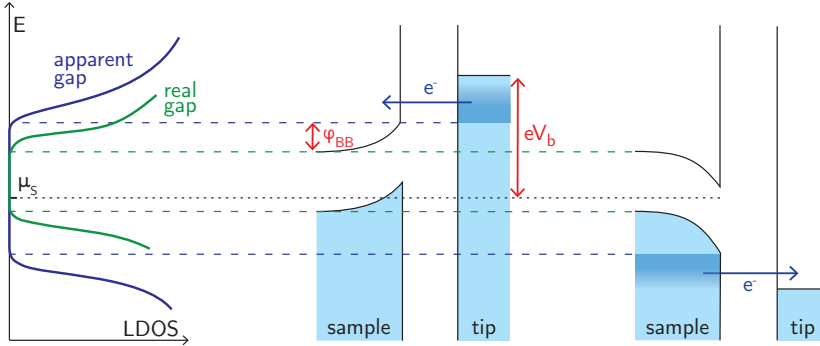


**Figure 5.1:** Schematic illustration of a tunneling spectroscopy experiment on a Mott insulator in absence (green) and presence (blue) of TIBB. The apparent gap measured with STM is bigger than the intrinsic gap of the material.

show how this can be attributed to the presence of field penetration in the material, and how we can correct for this phenomenon.

The main effect of field penetration is that the voltage between the tip and the sample surface directly below the tip no longer corresponds to the applied bias voltage  $V_b$ , but only to a fraction of it. It is relatively easy to qualitatively understand why this causes the measured STM gap to be bigger than the intrinsic gap in the sample LDOS. Let us consider in Fig. 5.1 how a scanning tunneling spectroscopy experiment is affected by the presence of TIBB. When acquiring a spectrum, the bias voltage  $V_b$  is swept while measuring the differential conductance  $dI/dV$ . In the case of a gapped LDOS as in a Mott insulator, the onset in the tunneling current occurs when the tip Fermi level crosses the lower boundary of the upper Hubbard band or the upper boundary of the lower Hubbard band. Both events occur at higher absolute bias voltages  $V_b$  in the presence of TIBB, as the bands bend upwards or downwards following the position of the tip Fermi level. Thus the apparent gap is wider than the real one when the tip electric field penetrates the sample.

In the following, we develop an algorithm that is able to retrieve the value of the intrinsic energy gap from the measured one. First, we need to calculate the value of the band banding potential  $\varphi_{BB}$  at the sample surface directly below the tip apex. For Mott insulators, this has never been done before: The models developed to calculate  $\varphi_{BB}$  in semiconductors [51] cannot be applied, since they require knowledge of the band structure, the carrier concentration and the dielectric constant, quantities that are not always available for Mott insulators. In Sec. 5.3.1, we introduce a model for electric field penetration in absence of free carriers that allows us to get an estimate of  $\varphi_{BB}$  by using the image charges method. Then, in Sec. 5.3.2, we use the obtained value of  $\varphi_{BB}$  as input parameter of an algorithm that allows us to retrieve the real

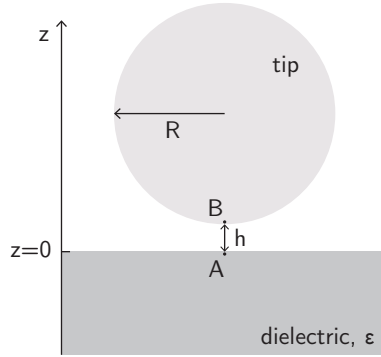


**Figure 5.2:** Schematic representation of the configuration used to calculate the band bending potential using the image charges method.

energy gap in the sample LDOS from the gap measured with STM, bridging the apparent contradiction with literature.

### 5.3.1 Calculation of the band-bending potential

Here, we develop a simple model of electric field penetration in the absence of free carriers that allows us to calculate the band-bending potential  $\varphi_{\text{BB}}$  for a lightly doped Mott insulator where important material parameters are unknown.

We consider the situation depicted in Fig. 5.2. As a first approximation, we model the tip as a conductive charged sphere of radius  $R$  at a distance  $h$  from the sample, where  $h \ll R$ , and the sample as a dielectric medium with dielectric constant  $\varepsilon$  filling a half-space. We consider a bias voltage  $V_b$  applied between the tip and the bottom of the sample, which is grounded. We need to find the band-bending potential  $\varphi_{\text{BB}}$  at the point of the sample closest to the tip (point A in Fig. 5.2), as a function of the bias voltage  $V_b$  applied to the tip.

In order to calculate the electric potential  $\varphi_{\text{BB}}$ , we make use of the image charges method [127]. In the simplest approximation of a uniformly charged sphere that can be replaced with a single point charge at the center of the sphere, an analytic expression for TIBB can be obtained:

$$\varphi_{\text{BB}}(V_b, R, h, \varepsilon) = \frac{1}{1 + \varepsilon \frac{h}{R}} \cdot (eV_b - W_0), \quad (5.1)$$

where  $W_0 = W_{\text{sample}} - W_{\text{tip}}$  represents the difference in work functions between sample and tip. In a more realistic configuration, the surface charge redistributes on the sphere. This problem has no analytical solution, and the expression for  $\varphi_{\text{BB}}$  has to

be found numerically by using an infinite series of converging image charges with diminishing absolute value<sup>1</sup>. The set of image charges is built in the following recurrent sequence: A charge  $q$  is added to the uncharged sphere, which is the equivalent of a point charge in the center of the sphere ( $q; R + h$ ). This point charge induces an image charge in the dielectric medium ( $-kq; -(R + h)$ ), where  $k = \frac{\varepsilon - 1}{\varepsilon + 1}$ . This in turn induces a dipole image on the sphere, ( $\frac{-kqR}{2(R+h)}; R + h$ ) and ( $\frac{-kqR}{2(R+h)}, r + h - \frac{R^2}{2(R+h)}$ ), and so on. The electric potential in the whole space is then given by

$$\varphi(\mathbf{r}) = \frac{\kappa}{4\pi\varepsilon_0} \sum_i \frac{q_i}{|\mathbf{r} - \mathbf{r}_i|}. \quad (5.2)$$

For  $z \geq 0$ ,  $\kappa = 1$  and  $(q_i, \mathbf{r}_i)$  are the initial charge and all the image charges induced on the sphere and in the sample. For  $z < 0$ ,  $\kappa = \frac{2}{1+\varepsilon}$  and  $(q_i, \mathbf{r}_i)$  are the initial charge and all the image charges induced on the sphere [127].

From Eq. (5.2), we can compute  $\varphi(\mathbf{r} = A)$ , which corresponds to the value of  $\varphi_{\text{BB}}$  at the point on the sample closest to the tip. Because the value of  $\varphi_{\text{BB}}$  depends on the bias voltage  $V_b$  applied to the tip, we also compute the potential at  $\varphi(\mathbf{r} = B)$ . We can then extract the proportionality constant between  $\varphi_{\text{BB}}$  and  $V_b$  from the ratio of this two potentials,

$$F(R, h, \varepsilon) = \frac{\varphi(\mathbf{r} = A)}{\varphi(\mathbf{r} = B)}, \quad (5.3)$$

obtaining finally the following expression for  $\varphi_{\text{BB}}$ :

$$\varphi_{\text{BB}}(V_b, R, h, \varepsilon) = F(R, h, \varepsilon) \cdot (eV_b - W_0). \quad (5.4)$$

The value of  $\varphi_{\text{BB}}$  therefore depends on the tip radius  $R$ , the tip-sample distance  $h$ , the static dielectric constant of the sample  $\varepsilon$  and the difference in work functions between sample and tip. In order to calculate  $\varphi_{\text{BB}}$ , we fix the values of  $R$  and  $\varepsilon$  to realistic parameters of our experiment. Using SEM, we measure typical radii  $R$  for our tips of 25 nm. We estimate the static dielectric constant of a typical Mott insulator as  $\varepsilon = 30$  (based on Ref. [128] for  $\text{La}_2\text{CuO}_4$  and Ref. [129] for  $\text{Sr}_2\text{IrO}_4$ ). We assume that this value can still be applied in the case of a very low doping concentration of  $\approx 2\text{--}3\%$  extra holes or electrons.

We further make use of finite element analysis (FEA) performed with the software package Comsol [60], first to confirm the results obtained with the image charges method on the simplified geometry, and second to estimate how different these results are in a more realistic geometry. In the latter, the tip is modeled as a cone with aperture of  $20^\circ$  ending with a spherical segment with the same tip radius  $R$ . The two configurations computed with FEA are represented in Fig. 5.3, where the calculated equipotential lines are shown.

---

<sup>1</sup>We verified that the simplified situation of a uniformly charged sphere underestimates  $\varphi_{\text{BB}}$  by a factor of two for our setup, requiring to take the full charge redistribution into account.

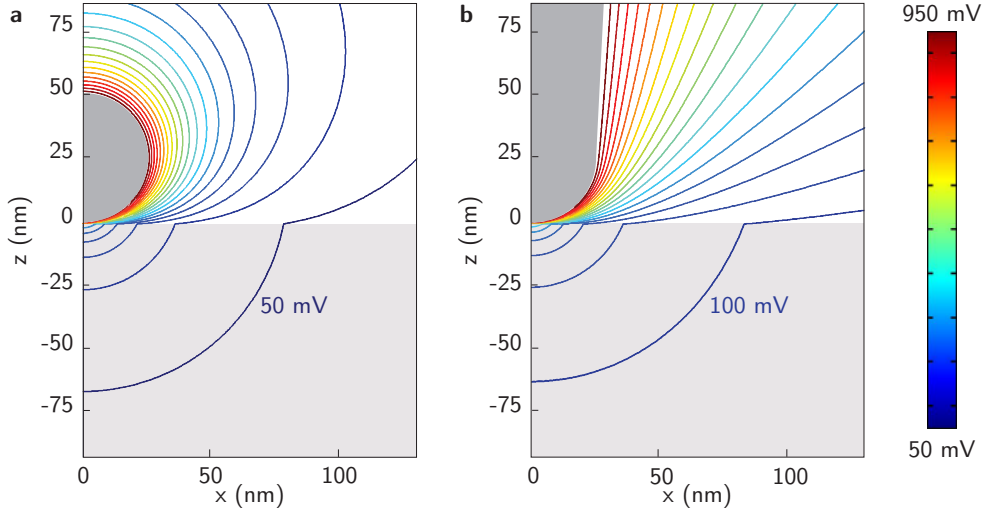


**Figure 5.3:** Result of FEA performed with Comsol [60] showing the electrical potential around tip and sample. **a**, Simplified spherical tip geometry. **b**, Conical tip geometry. In both panels, the tip-sample distance is set to  $5 \text{ \AA}$  and the equipotential lines, emphasizing the electric field penetration in the sample, are equally spaced by  $50 \text{ mV}$ . The equipotential line at  $50 \text{ mV}$  in panel **b** is not visible, because it is deeper below the surface of the sample.

In Table 5.1, we report the values of  $F(R, h, \varepsilon)$  obtained from the image charges method and from the two configurations calculated with FEA for a selection of tip-sample distances (where for simplicity we set  $W_0 = 0$ ). The image charges method results agree within 1% accuracy with FEA results performed on the same simplified geometry, and if the more realistic geometry is taken into account, the value of  $\varphi_{\text{BB}}$  increases by  $\approx 10\%$ . We can therefore conclude that our approximation of a spherical tip yields reasonable results.

$h$ ( $\text{\AA}$ )	image charges	FEA sphere	FEA cone
3	0.430	0.426	0.457
5	0.354	0.353	0.388
7	0.309	0.309	0.346

**Table 5.1:** Values of  $F(R, h, \varepsilon)$  obtained for three different tip-sample separations  $h$  from different methods: image charges method, FEA on spherical tip geometry, FEA on conical tip geometry.

### 5.3.2 Algorithm to retrieve the real energy scales in the LDOS

After obtaining the expression for  $\varphi_{\text{BB}}$  in Eq. (5.4), we can use it to extract the native density of states from the STM spectra. In addition to the calculated value of  $\varphi_{\text{BB}}$ , our algorithm needs as input parameters a series of  $dI/dV$  spectra measured at the same location with different tip-sample distances (fixed  $V_s$  and varying  $I_s$  covering at least one order of magnitude) and an  $I(z)$  spectrum.

Measuring a series of spectra with different set-up conditions can already give an indication for the presence of TIBB (even though it usually cannot rule it out). Figure 5.4a shows a series of  $dI/dV$  spectra measured subsequently at the same location with increasing tip-sample distances on a  $(\text{Sr}_{1-x}\text{La}_x)_2\text{IrO}_4$  sample with 2.2% doping. The setup bias voltage is kept constant at  $V_s = 1.5$  V and the setup current  $I_s$  ranges from 600 pA to 10 pA, covering almost two orders of magnitude. A clear dependence on the setup conditions, reflecting a dependence on the tip-sample distance, is visible.

We can calculate  $G = dI/dV$  in the presence of TIBB by taking the derivative with respect to  $V_b$  of Eq. (2.12):

$$G(V_b, h) = \frac{4\pi e^2}{\hbar} \left( 1 - \frac{\partial \varphi_{\text{BB}}(V_b, h)}{\partial V_b} \right) |M(h)|^2 g_t g_s (eV_b - \varphi_{\text{BB}}(V_b, h)). \quad (5.5)$$

The tip-sample distance  $h$  is mainly included in the unknown tunneling matrix elements  $|M(h)|^2$ . Following Ref. [23], we eliminate  $|M(h)|^2$  by normalizing the differential conductance  $G(V_b, h)$  by the setup current divided by the setup voltage:

$$\bar{G}(V_b, h) \equiv \frac{G(V_b, h)}{I_s/V_s}. \quad (5.6)$$

In absence of TIBB,  $\bar{G}$  would become independent of  $h$ , and such normalized spectra should collapse on a single curve. We apply Eq. (5.6) to the data in Fig. 5.4a, plotting the result in Fig. 5.4b: the curves do not collapse exactly on each other, the biggest differences arising for negative energies (see arrow). We quantify this difference by the standard deviations calculated for each energy, shown as the gray line in Fig. 5.4b. The differences in the normalized spectra are due to the presence of TIBB and thus further modeling is required to extract the intrinsic sample LDOS.

To do so, we calculate an effective bias voltage  $V^{\text{eff}}(h)$  for each tip-sample distance  $h$  such that

$$eV_s - \varphi_{\text{BB}}(V_s, h) \equiv eV^{\text{eff}}(h) - \varphi_{\text{BB}}(V^{\text{eff}}(h), h_0) \quad (5.7)$$

for a fixed tip-sample distance  $h_0$ .

Using Eq. (5.7), we rewrite the tunneling equation Eq. (2.12) as:

$$\int_0^{eV_s - \varphi_{\text{BB}}(V_s, h)} g_s(\epsilon) d\epsilon = \frac{I(V^{\text{eff}}(h), h_0)}{\frac{4\pi e}{\hbar} |M(h_0)|^2 g_t}. \quad (5.8)$$

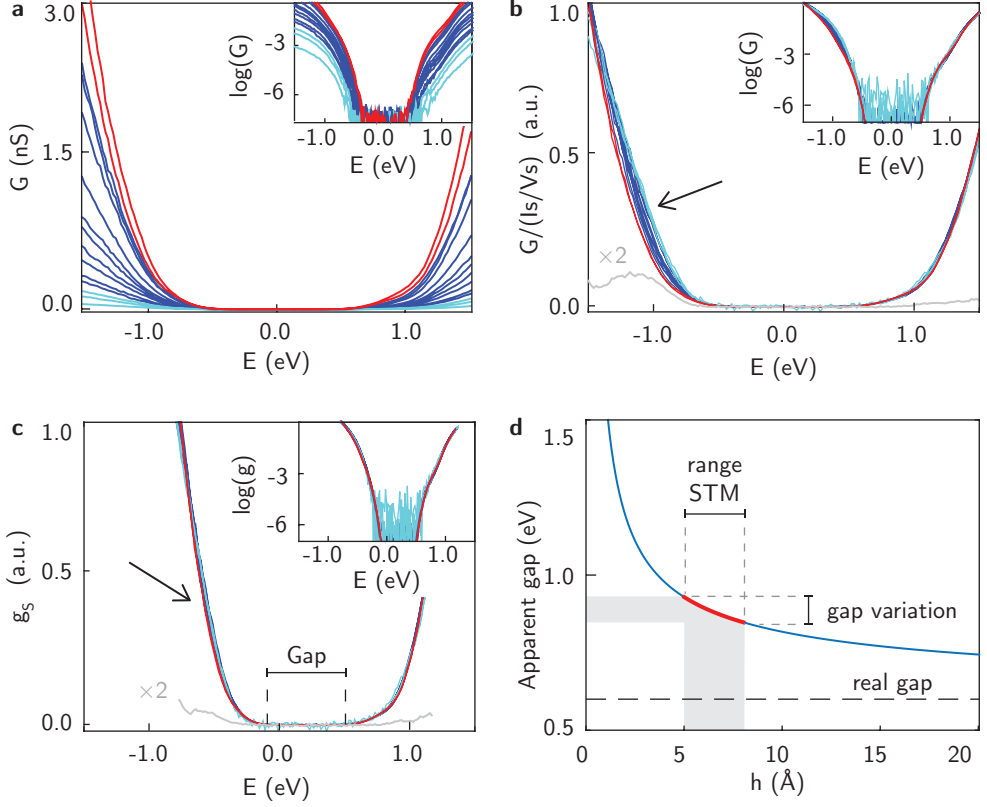


**Figure 5.4:** **a**,  $G \equiv dI/dV$  spectra measured at different tip-sample distances  $h$  on a sample with 2.2% doping. The bias setup voltage  $V_s$  is fixed to 1.5V and the current  $I_s$  goes from 600 pA (red) to 10 pA (light blue). In all insets the corresponding plot is shown on a logarithmic scale. **b**, The same spectra as in panel **a**, each normalized by its setup junction resistance  $I_s/V_s$ . The gray line shows the standard deviation  $\sigma(G)$  calculated for each energy, multiplied by a factor two. **c**, Intrinsic LDOS  $g_s$  after correction for TIBB, obtained from Eq. (5.9). Since the rescaling of the curves causes different horizontal axes for each curve, we calculate  $\sigma(g_s)$  over extrapolated values of  $g_s$  at equally spaced energies. **d**, Calculated apparent gap as a function of tip-sample distance.

By inserting Eq. (5.8) into Eq. (5.5) divided by the setup conditions, we can extract the intrinsic density of states  $g_s(\epsilon)$  from measured  $G(h)$  curves at different heights:

$$g_s(\epsilon) = \frac{G(h)}{I_s/V_s} \frac{1}{1 - \frac{\partial \varphi_{\text{BB}}(V_b, h)}{\partial V_b}} \frac{I(V^{\text{eff}}(h), h_0)}{\frac{4\pi e^2}{\hbar} |M(h_0)|^2 g_t}, \quad (5.9)$$

where  $\epsilon = eV_b - \varphi_{\text{BB}}(V_b, h)$ . The parameters in the model are the dielectric constant  $\epsilon$ , the tip radius  $R$ , the difference in work functions  $W_0$ , the minimal tip-sample distance  $h_{\text{min}}$  and the exponential prefactor  $\kappa$  of the tunneling current  $I = I_0 \cdot e^{-\kappa h}$ .

We keep  $R$  and  $\varepsilon$  fixed at the values mentioned in Sec. 5.3.1. We estimate  $h_{\min} = 5 \text{ \AA}$  as a typical tunneling distance for  $1 \text{ G}\Omega$  tunneling resistance for this material. From measured  $I(z)$  curves, we determine  $\kappa = 1.1 \text{ \AA}^{-1}$ . Thus the only free parameter left in Eq. (5.9) is  $W_0$ .

We apply our model to the data of Fig. 5.4a, extracting the parameter  $W_0$  as the value that minimizes the error function  $\Omega = \int [\sigma(g_s)]^2$ , where  $\sigma(g_s)$  are the standard deviations of the  $g_s$  curves for each energy. Minimization gives a work function difference between tip and sample of  $W_0 = 0.55 \text{ eV}$ .

We show in Fig. 5.4c the result of the application of our model to the data. The resulting spectra are rescaled in energy, leading to a gap value of  $600 \text{ meV}$  and to a shift of the onset of the lower Hubbard band to  $-0.1 \text{ eV}$ . This is in good agreement with values reported in literature by optical spectroscopy, theory and ARPES [71, 73, 77–79], allowing us to reconcile our measurement to the other techniques.

In Fig. 5.4d, we show the calculated evolution of the apparent gap with tip-sample distance. While there is a remarkable difference between the intrinsic gap value and the apparent gap, we want to stress that, within the values of  $h$  in which STM experiments are typically conducted, the variation of the apparent gap is relatively small. Therefore, even when measurements do not show sizable dependence on setup conditions, TIBB might be present, and further analysis might be required to retrieve the intrinsic energy scales.

## 5.4 Bubbles in the conductance layers of $(\text{Sr}_{1-x}\text{La}_x)_2\text{IrO}_4$

In the samples with higher doping levels ( $x \approx 5\%$ ), we observe a different signature of field penetration: circular rings of enhanced conductance appear in the layers of constant energy of the spectroscopic maps. In the following, we will refer to these features as ‘bubbles’. Their diameter increases with energy, as shown in Fig. 5.5a-d, causing hyperbolas of enhanced conductance in a  $(E, r)$  plot, as shown in Fig. 5.5e. We shall see that these bubbles are generated by the presence of a low concentration of specific impurity atoms which can be used as a probe to better understand the field penetration in the material.

Very similar features have been observed in semiconductors, where they are identified as markers of ionization/empty state filling of donors or acceptors induced by the vicinity of the STM tip. ‘Bubbles’ in semiconductors have been thoroughly studied because they can help in extracting material parameters such as the binding energy of the donors. This was done for instance for Si donors in GaAs [124, 125], for which it was further demonstrated that donors closer to the surface have an enhanced binding energy with respect to the bulk [130]. Effects of charge manipulation by the STM tip

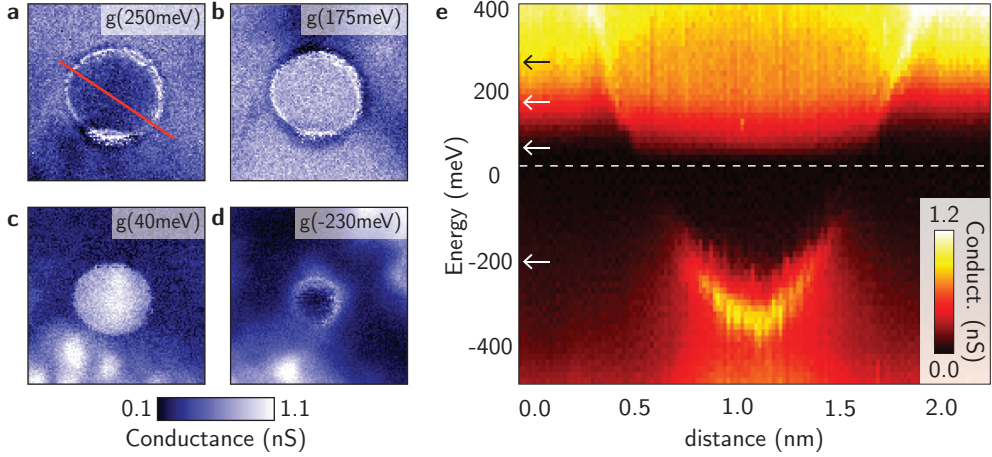


**Figure 5.5:** Visualization of a tip-induced band bending bubble in  $(\text{Sr}_{1-x}\text{La}_x)_2\text{IrO}_4$  at  $x=5.5\%$ . **a-d**, Conductance layers in a field of view of  $3 \times 3 \text{ nm}^2$  at 250 meV, 175 meV, 40 meV, -230 meV, respectively. **e**,  $(E,r)$  plot of the bubble along the red line in **a**. The hyperbolic profile visualizes the increasing diameter of the bubble with increasing energy. The arrows indicate the energies at which the conductance layers shown in panels **a-d** are extracted.

and enhanced binding energy closer to the surface were also reported for Mn acceptors in InAs and GaAs [121, 131] and for donors in ZnO [132, 133]. Moreover, bubbles due to TIBB effects have also been reported when using a scanning capacitance probe to image transport in two-dimensional electron gas in AlGaAs/GaAs heterostructures [134]. Despite semiconductors being relatively simple and accessible systems, the physics governing the appearance of the bubbles is quite complicated, and many details are not yet agreed upon.

We note that signatures of finite field penetration resembling the bubbles observed in our samples are also found in other correlated-electron systems, such as the lightly hole-doped oxychloride  $\text{Ca}_2\text{CuO}_2\text{Cl}_2$  [103] and possibly the correlated iridates  $\text{Sr}_3\text{Ir}_2\text{O}_7$  and  $\text{Sr}_3(\text{Ir}_{1-x}\text{Ru}_x)_2\text{O}_7$  [98, 117, 135]. However, these bubbles have never been discussed in details for a correlated-electron system.

We expect that the mechanism leading to the formation of bubbles in our samples is the same as in semiconductors, and we refer to Ref. [124, 125] for a detailed description of the processes.

Here, we emphasize that the impurity atoms in our samples are identified as electron donors, that each of these donors generates one hyperbola as in Fig. 5.5d, and that the two parts of the hyperbola lying above and below the chemical potential come from two different tunneling processes. For  $V_b > 0$ , the enhanced conductance is due to the ionization of the donor, which locally changes the potential landscape in the sample.

In this process, the electrons tunnel from the tip to the bulk of the sample, therefore the bubble becomes visible only after the onset of the upper Hubbard band. For  $V_b < 0$ , the enhanced conductance is instead caused by the opening of an additional tunneling channel. In this process, electrons tunnel from the sample bulk to the tip via the donor state. The bubble's diameter in this part of the hyperbola reflects the extension of the donor wave function in real space. Both processes are triggered at a specific value of  $\varphi_{\text{BB}}$ , causing the hyperbola to follow a constant  $\varphi_{\text{BB}}$  contour. We emphasize that the two parts of the hyperbola will lie on the same constant  $\varphi_{\text{BB}}$  contour only when the sample chemical potential roughly coincides with the onset of the upper Hubbard band, otherwise they might be shifted in energy.

In a typical spectroscopic map, we can usually identify several bubbles which start to emerge at different energies. Figure 5.6a shows the topograph of a  $17 \times 17 \text{ nm}^2$  field of view with doping level of 5.5%, where we count 180 dopant atoms on the surface. In the same field of view, the conductance layers show the appearance of only  $\approx 15$  bubbles (Fig. 5.6b). In general, the number of bubbles that we observe corresponds to less than 10% of the total number of La dopants present on the surface. We can therefore exclude that La dopants in their normal state cause the appearance of bubbles. Our best hypothesis on the nature of the bubbles is that they originate either from some special chemical state of the La atoms (for instance an oxygen vacancy next to the La atom) or from Pt atoms that substitute for the Ir atoms. The latter could originate from the Pt crucible where the samples were grown.

Even if the origin of the bubbles is not certain, from their presence and behavior we can still extract useful information about the material. Importantly, the bubbles are not influenced by and do not influence the phase-separated density of state of the sample. In Fig. 5.6b, we show the conductance layer at  $E = 540 \text{ meV}$  where the black contour indicates the border between pseudogap phase and Mott phase, as defined by the Mott parameter (see Sec. 4.6). The bubbles originate from both Mott regions and pseudogap regions, and when they cross the sharp border between the two regions their shape is not affected. Moreover, the phase-separated landscape and the emerging order that we describe in section 4.6 are not influenced by the presence of the bubbles.

Unfortunately, the model that we developed for the low doping level samples is unable to grasp the physics of the samples with doping  $x \approx 5\%$ , due to the presence of free carriers in the latter case. We can still make some important qualitative observations by plotting in Fig. 5.6c all the hyperbolas extracted from the bubbles in Fig. 5.6b:

(i), The bubbles start to appear at different threshold potentials. The threshold potential is an indication of the donor depth below the surface [130], with donors that lie deeper below the surface having a lower threshold potential. We therefore conclude that we observe bubbles originating from donors located at different depths.

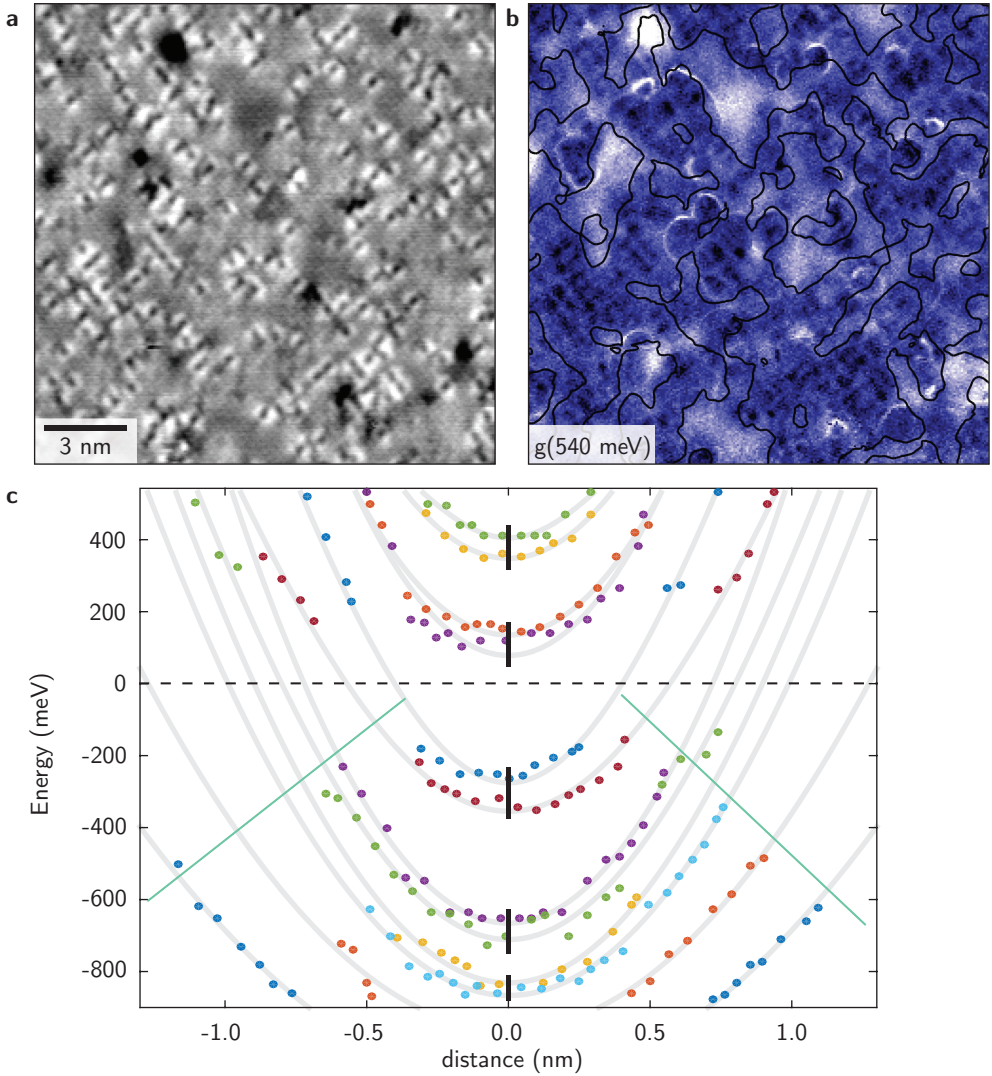


**Figure 5.6:** **a**, Topograph of a sample with  $x=5.5\%$  doping in a field of view of  $17 \times 17 \text{ nm}^2$  (same FOV as in Fig. 4.5). The setup conditions are ( $V_s = 460 \text{ meV}$ ,  $I_s = 300 \text{ pA}$ ). **b**, Conductance layer at  $540 \text{ meV}$  in the same field of view. We observe  $\approx 15$  circular bubbles of different sizes. The black line indicates the phase separation according to the Mott parameter defined in Sec. 4.6. **c**, Hyperbolas extracted from all the bubbles appearing in panel **b**. The gray lines are fits to the hyperbolas, added as a guide to the eye. The two green straight lines emphasize the increasing maximal bubble diameter with increasing donor depth below the surface. The vertical black lines group hyperbolas appearing at similar threshold potentials.

(ii), For the lower part of the hyperbola, the maximum bubble's diameter gets smaller for donors closer to the surface. Since the maximum diameter reflects the real space extension of the donor wave function, this gives evidence for enhanced binding energy for donors closer to the surface [130].

(iii), Most of the bubbles can be grouped as starting at roughly the same threshold potential (within an error of 50 meV), therefore probably originating from donors at the same depth below the surface, i.e. belonging to the same crystal layer. In Fig. 5.6c this is indicated by the short vertical black lines.

Concluding, we would like to emphasize a last important point that might tell us something more about the material. The typical lateral extension of the bubbles in our samples is  $\approx 1.5$  nm. This is significantly lower than in semiconductors where, for example, the typical extension of bubbles due to Si donors in GaAs is  $\approx 10$  nm. Among the factors that can influence the extension of the bubbles are the tip radius, the concentration of free carriers and the material's electrical permittivity. We can exclude that the tip radius is the cause for the small extension of the bubbles, as one would need to have an unrealistically small tip radius to reproduce the bubbles. We identify two factors that could be responsible for the reduced lateral extension of the bubbles: (i) the resistivity in  $(\text{Sr}_{1-x}\text{La}_x)_2\text{IrO}_4$  is lower in the ab-crystal plane than along the c-axis [129], although with diminishing strength upon doping [91]; (ii) the electrical permittivity of  $\text{Sr}_2\text{IrO}_4$  is anisotropic [129]. We can only speculate that the small extension of the bubbles is related to these effects; in any case it is evidence for the strongly anisotropic electronic structure of the material.

## 5.5 Conclusions

In this chapter, we showed that electric field penetration in materials with poor electronic screening can strongly influence STM results.

It is important to be aware of the possibility to encounter TIBB when performing experiments on lightly doped Mott insulators and other materials with poor electronic screening (including topological materials [136] and van der Waals heterostructure; magic-angle superconducting graphene [137] would likely be affected by this effect). The presence of TIBB could be difficult to identify, and one has to be extra careful when measuring such materials. The appearance of bubbles in the conductance layer can and should be used as an indication for the presence of TIBB in the sample.

In particular, we showed that the incompatibilities between STM and other techniques in the gap value measured on  $(\text{Sr}_{1-x}\text{La}_x)_2\text{IrO}_4$  for  $x < 4\%$  are caused by field penetration. We developed a model to correct for this effect that can generally be applied to lightly doped Mott insulators. We showed that, after correcting the data

according to this model, our STM results reconcile with literature. We would like to emphasize that what is discussed in this chapter does not influence the findings of chapter 4. Even though the gap values for the low doping samples as reported in chapter 4 do not correspond to the intrinsic values, our interpretation of the physics of the material is not affected.

